

# Probing Lithium Germanide Phase Evolution and Structural Change in a Germanium-in-Carbon Nanotube Energy Storage System

Wei Tang,<sup>†,||</sup> Yanpeng Liu,<sup>†</sup> Chengxin Peng,<sup>†</sup> Mary Y. Hu,<sup>‡</sup> Xuchu Deng,<sup>‡</sup> Ming Lin,<sup>\*,§</sup> Jian Zhi Hu,<sup>\*,‡</sup> and Kian Ping Loh<sup>\*,†</sup>

<sup>†</sup>Department of Chemistry and Graphene Research Centre, National University of Singapore, 3 Science Drive 3, Singapore 117543

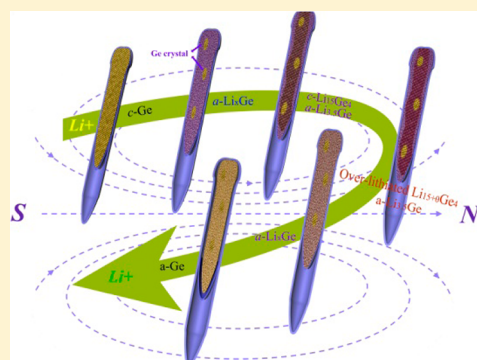
<sup>‡</sup>Pacific Northwest National Laboratory, Richland, Washington 99354, United States

<sup>§</sup>Institute of Materials Research and Engineering, A\*STAR (Agency for Science, Technology and Research), 3 Research Link, S117602, Singapore

<sup>||</sup>Graduate School for Integrative Sciences and Engineering, National University of Singapore, 28 Medical Drive #05-01, Singapore 117456

## S Supporting Information

**ABSTRACT:** Lithium alloys of group IV elements such as silicon and germanium are attractive candidates for use as anodes in high-energy-density lithium-ion batteries. However, the poor capacity retention arising from volume swing during lithium cycling restricts their widespread application. Herein, we report high reversible capacity and superior rate capability from core–shell structure consisting of germanium nanorods embedded in multiwall carbon nanotubes. To understand how the core–shell structure helps to mitigate volume swings and buffer against mechanical instability, transmission electron microscopy, X-ray diffraction, and *in situ* <sup>7</sup>Li nuclear magnetic resonance were used to probe the structural rearrangements and phase evolution of various Li–Ge alloy phases during (de)alloying reactions with lithium. The results provide insights into amorphous-to-crystalline transition and lithium germanide alloy phase transformation, which are important reactions controlling performance in this system.



## INTRODUCTION

Group IV elements such as tin (Sn),<sup>1–3</sup> germanium (Ge),<sup>4–10</sup> and silicon (Si),<sup>11–17</sup> with theoretical capacities of 992, 1623, and 4200 mAh g<sup>-1</sup> respectively, are attractive alternatives to carbon-based anodes in lithium-ion batteries (LIBs). Despite having a lower capacity than Si, Ge has 400 times higher diffusivity of lithium and 1 × 10<sup>4</sup> times higher electrical conductivity and thus has advantages for use in high-power LIBs for electrical vehicles and large energy-storage stations.<sup>18–24</sup> However, similar to Si, drastic volume changes (370%) during lithiation and delithiation, together with the loss of electrical contact or unstable formation of surface SEI film arising from these, result in rapid capacity decay.<sup>18</sup> Strategies to mitigate these problems generally involve nanostructuring the Ge to minimize volume swing and embedding it on an electrically conducting scaffold such as amorphous carbon or reduced graphene oxide to buffer against mechanical instability and enhance the rate capability.<sup>6,8,9,17,25–33</sup> Despite the enhanced performance, the inevitable inhomogeneity of these carbon coatings in physically mixed systems negatively affects the capacity retention and rate capability of the system.<sup>5</sup> Recently “core–shell structure” such as Ge NWs (core)/carbon (shell) as a generic concept has emerged as a favored material design in energy storage system.<sup>5,34,35</sup> The common route to

synthesize such core–shell structure is based on a post-carbon-coating method on the as-prepared Ge NWs. Metal-seeded vapor–liquid–solid (VLS),<sup>5,36,37</sup> supercritical fluid–liquid–solid (SFLS),<sup>34,38</sup> solution–liquid–solid (SLS), and metal–organic chemical vapor deposition (MOCVD) have been applied to synthesize Ge NWs.<sup>9,35,36,39,40</sup> Conventional VLS-type CVD suffers from low synthetic yield due to safety concerns which require the GeH<sub>4</sub>/GeCl<sub>4</sub> precursors to be operated at very dilute concentrations. Using solution-phased SFLS and SLS methods, the production can be scaled up to gram level. However, the high operation pressure in SFLS and requirement of high boiling point reaction solvents in SLS hinder upward scaling.<sup>36</sup> Using liquid organometallic compounds as precursors, MOCVD approach is capable of scaling up the production of Ge NWs more safely and economically.<sup>36</sup> As-prepared Ge NWs/NRs (nanorods) were modified with carbon-based protection layer to improve their electrochemical performance.

Despite the rapid progress on the material engineering of Ge core–shell structure, the mechanism of reaction of Ge in lithium cycling remains unclear, which makes attempts to

Received: November 19, 2014

Published: February 3, 2015

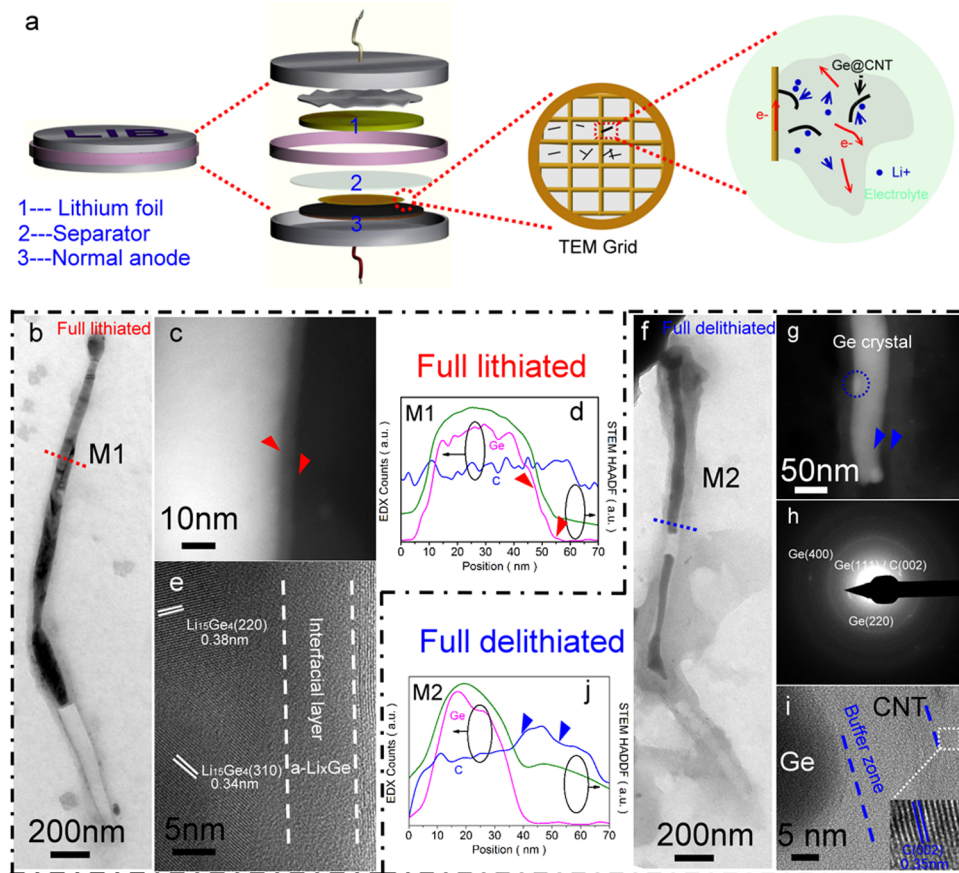


**Figure 1.** Structural change in the Ge@CNT composite during the first lithiation/delithiation cycle. (a) Illustration of the TEM coin-cell configuration. (b and e) TEM and (c) STEM images of the Ge@CNT composite, and (d) Elemental profile acquired by STEM EDX across line M1 in the Ge@CNT composite at full lithiation, an interfacial layer with reduced Ge density is indicated by the red arrows. (f and i) TEM and (g) STEM images of the Ge@CNT composite at full delithiation. (h) SAED pattern for the Ge@CNT composite, showing that it is amorphous with Ge crystalline “islands” dispersed within. (j) Elemental profile acquired by STEM EDX across line M2 in the Ge@CNT composite at full delithiation, where a buffer zone is indicated by the blue arrows. At full lithiation there is a 10 nm interfacial layer between the Ge NRs and the carbon layers, with a lower Ge density based on STEM and elemental mapping. At full delithiation, parts of the Ge NRs contract from the carbon layers, and a buffer zone is created.

optimize performance based on electrochemical–structural correlations difficult. The problem is compounded by the amorphous nature of the lithium germanide phases,<sup>7,35,41</sup> which precludes clear elucidation of the structural changes that occur during lithiation/delithiation using X-ray diffraction (XRD)<sup>42,43</sup> or electron microscopy (EM).<sup>44–48</sup> By providing detailed local structural information and detecting both crystalline and the amorphous phase simultaneously, nuclear magnetic resonance (NMR) spectroscopy can be combined with traditional methods to provide a powerful tool for elucidating the electrochemical–structural correlations.<sup>49–57</sup> Herein, we successfully develop a strategy to fabricate a capsule-like structure consisting of Ge nanorods encapsulated by bamboo-type multiwall carbon nanotubes (Ge@CNT), using Ge nanoparticles as seeds. The unique capsule-like compartment of Ge@CNT protects against volume swing and allows dynamic structural change and phase evolution (reversible amorphous-to-crystalline transition) of the Ge during lithiation/delithiation to be revealed by *in situ* <sup>7</sup>Li NMR and TEM. Unlocking phase evolution during Li alloying and dealloying in the lithium germanide systems shed light on the origin of the high-capacity Li storage and its reversibility.

## RESULTS AND DISCUSSION

**Synthesis and Electrochemical Performance of Ge@CNT.** Ge@CNT was prepared through a one-step CVD growth approach from Ge nanoparticle directly: A Ge nanoparticle/magnesium oxide catalyst (Ge NP/MgO) was first prepared by ball-milling magnesium (Mg) and germanium dioxide (GeO<sub>2</sub>) together, during which a solid-state reduction of GeO<sub>2</sub> resulted in the formation of Ge NPs coated with MgO. Supported on an alumina substrate, the composite was used to catalyze carbon nanotube (CNT) growth at 880 °C in a CVD furnace using a mixture of methane (CH<sub>4</sub>) and hydrogen (H<sub>2</sub>). After CVD, a high yield of the core (Ge) plus shell (CNT) structure was obtained; the Ge NPs were reshaped into nanorods around 1.5 μm long inside CNT walls with thickness of 5–10 nm. To suppress growth of amorphous carbon, water vapor was introduced by bubbling part of the reaction gases through distilled water during the growth process.<sup>58</sup> Carbon, hydrogen, nitrogen, and sulfur (CHNS) analysis showed that the Ge@CNT composite contained only ~5% by weight of carbon. As a control, bare Ge particles were obtained by using HCl to dissolve the MgO from the Ge NP/MgO composite directly after ball-milling. The detailed synthetic procedure, morphol-

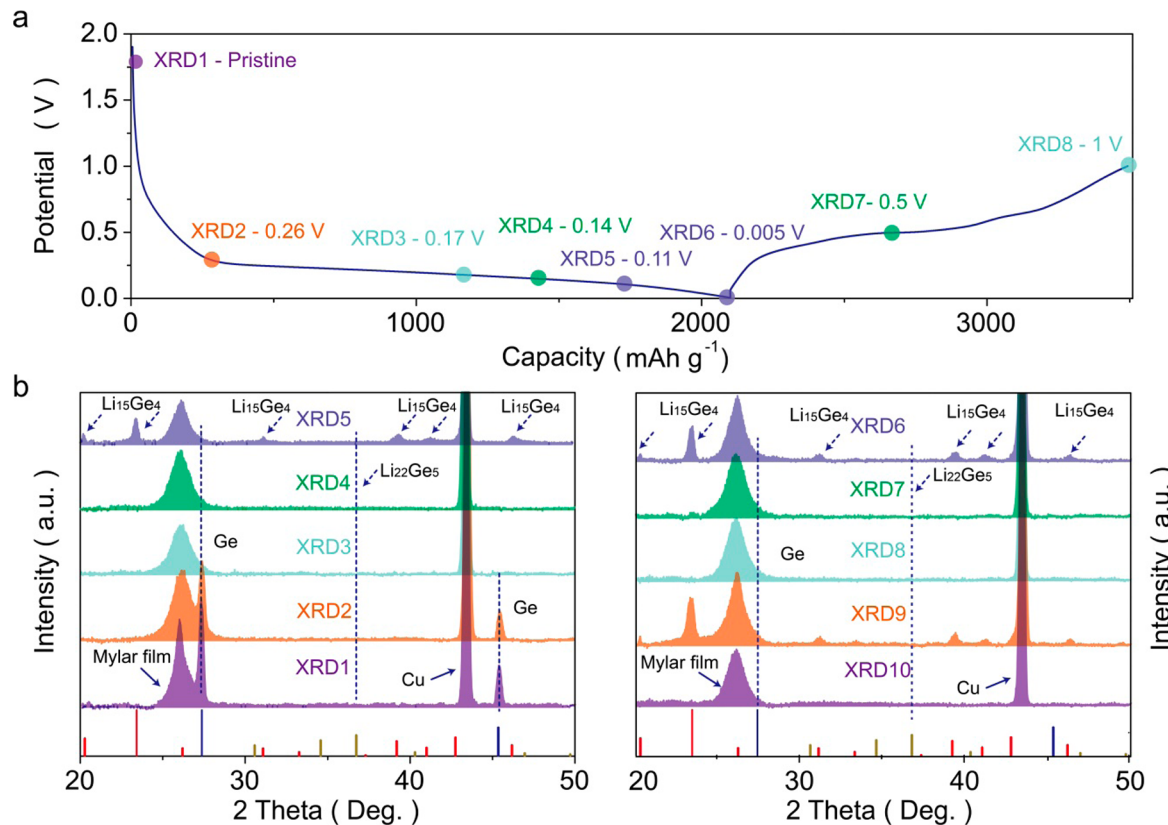


**Figure 2.** Reversible amorphous–crystalline transitions during the lithiation/delithiation of Ge@CNT. (a) First cycle voltage plot of Ge@CNT at 0.2C to indicate stages where XRD was measured. (b) Stacked X-ray diffraction patterns collected from Ge@CNT composite electrode during the first discharge/charge cycle (XRD1–XRD8), redissolve to 0.005 V (XRD9), and charge to 1 V after 200 cycles (XRD10). Reversible amorphous–crystalline transition is revealed during the lithiation and delithiation of Ge@CNT. There is no Li<sub>22</sub>Ge<sub>5</sub> crystalline phase shown in all the XRD spectra. The reference patterns for Li<sub>15</sub>Ge<sub>4</sub> (red; JCPDS card no. 89-3034), Ge (blue; JCPDS card no. 89-5011), and Li<sub>22</sub>Ge<sub>5</sub> (dark yellow; JCPDS card no. 17-0402) are indicated as bars in the Figure. The diffraction peaks of Mylar seal film and the Copper current collector are indicated in the figure.

ogy, and characterization of Ge@CNT and bare Ge have been added in Figure S1–S5.

When used as anode materials for LIBs, the Ge@CNT system can deliver promising performance. The detailed electrochemical characterizations and discussions are included in Figures S6–S12. The performance of this Ge@CNT system as anode for LIBs can be clearly seen in Table S1, in which the rate capability, capacity retention, and high specific capacity of the Ge@CNT composite are compared with previously reported Ge-based systems, including Ge coated with amorphous carbon or reduced graphene oxide,<sup>4–8,25,32–35,59–61</sup> and even one of the best performance nano Ge/rGO/C system reported to date.<sup>39</sup> In contrast, bare Ge exhibits poor electrochemistry beyond the first discharge, in part due to problems associated with maintaining electrical contacts between the bare Ge particles and the current collector (Figure S10).<sup>35</sup> This limitation precludes detailed and operando study of phase transition on Ge-based electrode during lithium cycling. In this report, the Ge@CNT structure provides an effective model for multiprobe studies (TEM, XRD and *in situ* NMR) as electrical contact was maintained throughout the lithium cycling.<sup>12</sup>

**Structural Change in the Ge@CNT Composite during Lithiation/Delithiation Using a TEM Coin-Cell Configuration.** Stress-induced pulverisation or unstable formation of surface SEI film due to volume swing has been reported to be the main cause of degradation in Ge-based batteries, and thus a

direct visualization of the rearrangement process may provide insights into stress points in the structure.<sup>4–10</sup> Herein, the structural changes in Ge@CNT during lithiation/delithiation were studied using a TEM coin-cell configuration.<sup>44,62</sup> As illustrated in Figure 1a, the Ge@CNT composite was first loaded onto a TEM grid, and the entire structure was then incorporated into a conventional coin cell, which was subjected to galvanostatic charging/discharging (0.2 C). The charge/discharge process was interrupted at different stages, and the TEM grids were disassembled from the cell for TEM characterization. This method minimizes damage to the sample during preparation, as direct viewing is possible without mechanical agitation or dispersion in solutions.

The TEM observations revealed a dynamic structural rearrangement of the Ge NRs during lithium cycling, with several salient features. The morphology of the Ge@CNT composite was well preserved throughout the lithiation (Figure 1b–d) and delithiation (Figure 1e–i) cycles.<sup>7,9,35</sup> The carbon sheath over the Ge ensured that electrical contact was maintained throughout the lithiation/delithiation processes. Second, rather than isotropic volume expansion, the confinement of the Ge within the carbon walls meant that some volume expansion occurred along the axis of the carbon wall, with the latter acting as a supporting scaffold.<sup>63</sup> In the initial discharging to 0.17 V, about half of the capacity was delivered, and the bulk of the Ge NRs were alloyed with Li<sup>+</sup> to become an amorphous Li<sub>2.26</sub>Ge phase (as later verified by NMR) (Figure

S13a,b). As shown in the TEM image in Figure 1e, at full lithiation the amorphous phase was transformed into a crystalline  $\text{Li}_{15}\text{Ge}_4$  phase (verified by ex situ XRD, as discussed below). As verified by STEM (Figure 1c) and elemental mapping (Figure 1d), a 10 nm-thick amorphous Li–Ge phase (indicated by red arrows to show Ge with a relative low distribution) was formed between the CNT walls and the crystalline  $\text{Li}_{15}\text{Ge}_4$  phase (also observed in previous in situ TEM study).<sup>48</sup> The coexistence of amorphous and crystalline phases is consistent with the high-angle annular dark field (STEM-HAADF) plot. Around the shoulder of HAADF plot (5–15 and 45–55 nm), the counts have reduced to the background level of CNT, indicating a relatively low Ge concentration in the amorphous phase.

Upon delithiation (charging to 0.5 V), the crystalline phase was converted back to a mostly amorphous lithium germanide phase (Figure S13c,d). Importantly, at the end of delithiation (charging to 1 V), a contraction of the dealloyed Ge from the carbon wall was apparent.<sup>63</sup> Figure 1g,h shows that the dealloyed Ge became largely amorphous, with several crystalline Ge “islands” dispersed within it. Similar to the mechanism proposed for the nucleation of amorphous Si clusters from existing seeds or defects, the presence of these Ge nanocrystals may act as seeds for the growth of amorphous Ge domains after  $\text{Li}^+$  have diffused away.<sup>64</sup> The amorphous Ge domains are believed to allow a more facile alloying reaction kinetics in subsequent cycles as it will be easier to achieve  $\text{Li}^+$  insertion in a loose Ge tetrahedral network.<sup>52</sup> According to the TEM image (Figure 1i) and the elemental mapping profile (Figure 1j), a 10 nm buffer zone (indicated by blue arrows to show empty carbon sheath without Ge; the plateau in HAADF plot, Figure 1j, around 40–50 nm with only background counts of CNTs is consistent with the emerging of buffer zone) was present throughout the lithiation and delithiation cycles and remained structurally similar when it was analyzed at the end of 200 cycles (Figure S14). This buffer zone is believed to accommodate the stress associated with volume change during (de)lithiation cycles.

**X-ray Diffraction Study of the Reversible Amorphous-to-Crystalline Transition in Ge@CNT Composite during Lithium Cycling.** According to previous XRD studies,<sup>43</sup> the lithiation mechanism in Ge occurs via four distinct crystal phases,  $\text{Li}_9\text{Ge}_4$ ,  $\text{Li}_7\text{Ge}_2$  and  $\text{Li}_{15}\text{Ge}_4/\text{Li}_{22}\text{Ge}_5$ , although XRD is not capable of detecting the presence of the amorphous alloy phase. To investigate the amorphous-to-crystalline transition of the Ge@CNT composite during lithium cycling, ex situ XRD analyses were performed at selected potentials as indicated in the first discharge/charge voltage plot (Figure 2a). At the first discharge to 0.17 V, the crystalline diffraction peaks of Ge (XRD1–XRD4, Figure 2b) vanished. At 0.11 V, near the end of discharge, peaks attributable to crystalline  $\text{Li}_{15}\text{Ge}_4$  phase appeared (XRD5). There were no new crystalline phases at the end of the discharge (XRD6). Upon delithiation, the crystalline phase was quickly converted to the amorphous phase at the charging stages of 0.5 V (XRD7) and 1 V (XRD8). At the end of the second discharge, the  $\text{Li}_{15}\text{Ge}_4$  crystalline phase was observed to reappear (XRD9). These observations suggest a reversible amorphous-to-crystalline transition during the lithium cycling of the Ge@CNT composite: upon first lithiation, crystalline Ge becomes amorphous, and at the end of the discharge it partly transforms into the crystalline  $\text{Li}_{15}\text{Ge}_4$  phase; upon delithiation, the crystalline  $\text{Li}_{15}\text{Ge}_4$  phase changes into amorphous  $\text{Li}_x\text{Ge}$  or Ge. As seen in the TEM images in

Figure 1e, amorphous and crystalline phases coexisted during the interconversion. Note that the reaction kinetics of the Ge@CNT composite were much faster than those of Si;<sup>18</sup> thus, after one cycle, almost all of the active mass involved in the electrochemical reaction became amorphous upon delithiation. In subsequent cycles, the reversible amorphous-to-crystalline transition between amorphous Ge and crystalline  $\text{Li}_{15}\text{Ge}_4$  continued during alloying and dealloying (XRD9, XRD10).

### In situ $^7\text{Li}$ NMR Study of the Lithium Germanide Alloy

**Phase Transformation in Ge@CNT.** To understand the detailed local structural evolution, an in situ  $^7\text{Li}$  NMR study was performed. An operando identification of the lithium germanide phases under various cycling regimes permits understanding of the kinetics of phase transition between different structural phases, including the amorphous phases and how these correlate with capacity retention. Combining data from TEM and in situ  $^7\text{Li}$  NMR, we discovered that the phase interconversion during cycling was mediated by coexisting amorphous and crystalline phases and that the high capacity observed was correlated with an overlithiated lithium germanide phase.

In situ  $^7\text{Li}$  NMR experiments on the Ge@CNT composite were performed at 0.2 C between 0.005 and 1 V. In Figures 3

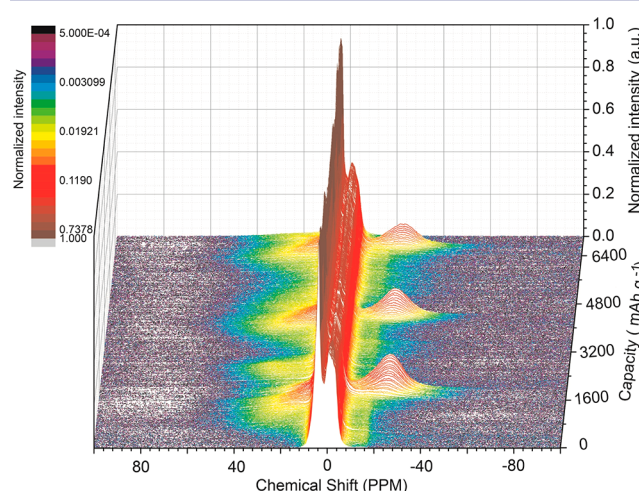
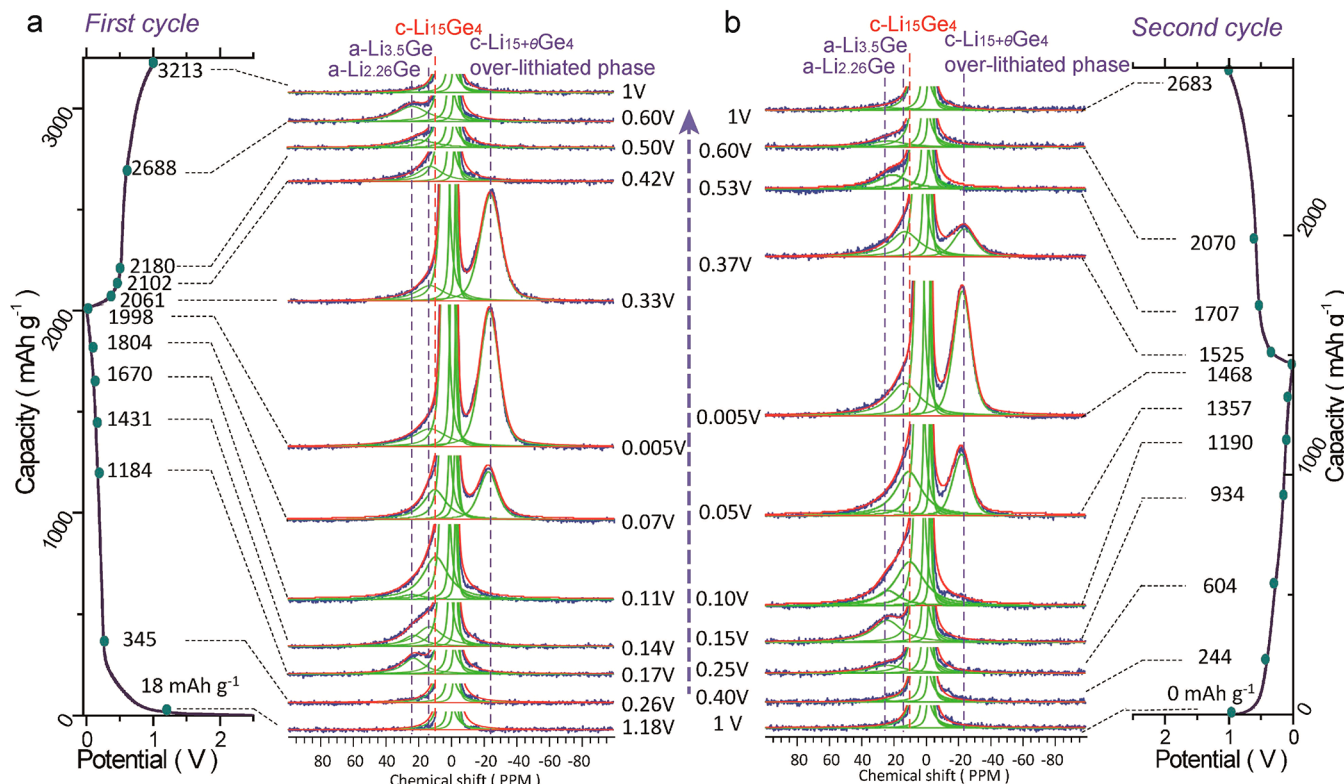


Figure 3. Color-mapped in situ  $^7\text{Li}$  NMR spectra of Ge@CNT during lithiation and delithiation cycles.

and 4, a series of in situ  $^7\text{Li}$  NMR spectra is plotted. Generally, four  $^7\text{Li}$  resonances, centered at 24, 13, 10, and –24 ppm (marked R1, R2, R3 and R4, respectively) were identified in addition to the  $^7\text{Li}$  resonance of the electrolyte and the SEI peak centered around 0 ppm (–3, –1, and +4 ppm).<sup>50,65</sup> As shown in Figure 3, the line width and line shape of the signals from electrolyte and SEI film are quite narrow and resolved, thus they can be separated from the  $\text{Li}_x\text{Ge}$  signals during the fitting. Most importantly, the signals from electrolytes and SEI are almost constant during the discharge–charge process (the experimental design, data fitting method, and quantitative analysis of the phase compositions following the methods of Eckert and Pöttgen, et al. are included in Figure S15 and Table S2).<sup>66,67</sup>

According to the evolution of resonance peaks R1–R4 (see Table 1) during the discharge/charge process, lithiation was judged to proceed in four stages as given in equation 1.

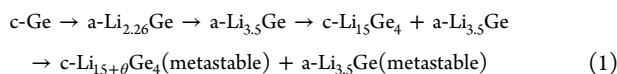


**Figure 4.** Stacked in situ  $^7\text{Li}$  NMR spectra of the Ge@CNT composite obtained during the first two galvanostatic charge/discharge cycles: (a) first and (b) second cycles. Along with the lithiation/delithiation cycles, four  $^7\text{Li}$  resonances centered at 24, 13, 10, and  $-24\text{ ppm}$  (marked R1, R2, R3, and R4, respectively) were identified and monitored together with the  $^7\text{Li}$  resonance of the electrolyte and that of the SEI centered around 0 ppm. The high Li-shield phase (R4) was attributed to an overlithiated  $\text{Li}_{15+\theta}\text{Ge}_4$  phase.

**Table 1. Summary of in Situ  $^7\text{Li}$  NMR Observations**

resonance index	assigned phase	chemical shift (ppm)	potential/capacity <sup>a</sup>	crystal property	observed by
R1	$\text{Li}_{2.26}\text{Ge}$	24	0.17/839	amorphous (in situ XRD <sup>42</sup> and TEM)	NMR (in situ $^7\text{Li}$ )
R2	$\text{Li}_{3.5}\text{Ge}$	13	0.14/1086		NMR (in situ $^7\text{Li}$ )
R3	$\text{Li}_{15}\text{Ge}_4$	10	0.11/1325	crystalline phase (in situ XRD <sup>42</sup> and TEM <sup>68,69</sup> )	NMR (in situ $^7\text{Li}$ ), in situ XRD <sup>42</sup>
R4	$\text{Li}_{15+\theta}\text{Ge}_4$	$-24$	0.005/1653	overlithiated	NMR (in situ $^7\text{Li}$ )

<sup>a</sup>The capacities of carbon lithiation and the initial formation of SEI passivation layers have been subtracted.



During the first discharge (Figure 4a), there was no obvious change in the spectra until 0.26 V due to carbon lithiation and the initial formation of passive SEI layers.<sup>50,52</sup> The R1 peak at 0.17 V was attributed to the amorphous a-Li<sub>2.26</sub>Ge phase or another early amorphous lithiated phase of Ge (as no XRD peaks were observed in the ex-situ study at this point and after the capacity of the carbon process and the initial formation of the SEI were subtracted:  $1184 - 345 = 839\text{ mAh g}^{-1}$ , equivalent to  $2.26\text{ Li}^+$  inserted per Ge, this phase agreed well with c-Li<sub>9</sub>Ge<sub>4</sub>).<sup>43</sup>

At around 0.14 V, an R2 peak emerged in the spectra, reflecting the transformation of a-Li<sub>2.26</sub>Ge to a-Li<sub>3.5</sub>Ge (based on the calculation of the peak area ratio of R1/R2 = 0.45 and the corresponding capacity). The phase was similar to the previous ex-situ XRD observation of c-Li<sub>7</sub>Ge<sub>2</sub>,<sup>43</sup> but our XRD study (Figure 2 XRD4) did not observe any crystalline phases, and hence we denote this as an amorphous phase. Upon discharging to 0.11 V, a new resonance R3 peak appeared at the

discharging capacity of  $1325\text{ mAh g}^{-1}$  ( $3.6\text{ Li}^+$  inserted per Ge). According to XRD (Figure 2) and TEM observations, this phase should be assigned to Li<sub>15</sub>Ge<sub>4</sub> ( $3.75\text{ Li}^+$  inserted per Ge).<sup>42</sup> After careful investigation of the NMR spectra, we did not find a pronounced peaking point for R2, indicating that transformation from Li<sub>2.26</sub>Ge to Li<sub>15</sub>Ge<sub>4</sub> through Li<sub>3.5</sub>Ge may be a nonlinear process. At the end of the discharge, a new resonance appeared at  $-24\text{ ppm}$  (R4) at 0.07 V, accompanied by a loss of R3 intensity, although ex situ XRD confirmed that an Li<sub>15</sub>Ge<sub>4</sub> crystalline structure was still present (Figure 2).<sup>42</sup> Peak R4 was strongest in intensity at the end of the discharge, at  $\sim 1653\text{ mAh g}^{-1}$ . We assigned R4 to the overlithiated phase Li<sub>15+</sub> $\theta$ Ge<sub>4</sub> ( $0 < \theta < 1$ , according to the second discharging capacity of  $1468\text{ mAh g}^{-1}$ ).<sup>18</sup> This assignment is analogous to overlithiated lithium silicide phases found previously.<sup>52</sup> At the end of the first discharge, we found that R2 reappeared in the spectra accompanied by the vanishing of R3. We believe that the conversion of the a-Li<sub>3.5</sub>Ge phase to the c-Li<sub>15</sub>Ge<sub>4</sub> phase is incomplete during lithiation. The stoichiometric phase of Li<sub>3.6</sub>Ge at 0.11 V consists of both Li<sub>3.5</sub>Ge and Li<sub>15</sub>Ge<sub>4</sub> phases, suggesting that there may be a kinetic barrier to Li<sub>15</sub>Ge<sub>4</sub>.

(crystalline phase) formation from  $\text{Li}_{3.5}\text{Ge}$  (amorphous phase).<sup>52</sup> We believe that formation of crystalline cluster phase would require not only Ge–Ge bond breakage but also the rearrangement of Ge (Ge migration), which involves a large active barrier.<sup>64</sup> At the end of lithiation, the electrode material should be a mixture of the a- $\text{Li}_{3.5}\text{Ge}$  phase and the overlithiated phase c- $\text{Li}_{15+\theta}\text{Ge}_4$  (see Figure 1e, a TEM image of the grid discharged to 0.005 V) rather than single crystalline  $\text{Li}_{15}\text{Ge}_4$  or overlithiated  $\text{Li}_{15+\theta}\text{Ge}_4$  phases.<sup>42,51,52</sup> The existence of a- $\text{Li}_{3.5}\text{Ge}$  may further reduce the kinetic barrier for the transformation of c- $\text{Li}_{15+\theta}\text{Ge}_4$  to a- $\text{Li}_x\text{Ge}$  upon delithiation,<sup>64</sup> which helps to reduce the “overpotential” between lithiation and delithiation.

In the charging process, the R4 peak disappeared completely by 0.42 V, while the R2 resonance became pronounced. Before the end of delithiation, the resonance shifted to high frequencies at R1, indicating a rapid delithiation process in a short potential window (see the sharp oxidation peak in CVs in Figure S6a). In the second cycle (Figure 4b), the phase transformation appeared to be similar to the first cycle except that R1 ( $\text{Li}_{2.26}\text{Ge}$ ) occurred at a somewhat more positive potential during lithiation (0.25 V), and R4 ( $\text{Li}_{15+\theta}\text{Ge}_4$ ) was converted to R2 ( $\text{Li}_{3.5}\text{Ge}$ ) more rapidly upon delithiation (0.005–0.37 V). These differences may be attributed to the amorphous property of Ge upon delithiation (see Figure 1g,h,i), which speeds up the reaction kinetics of (de)-lithiation.<sup>52,70</sup>

Interestingly, peaks R2 and R4 in the  $^7\text{Li}$  NMR spectra at 0.005 V at the end of the second and third lithiations (0.005 V, Figure 5i) appeared to interconvert in a highly reversible manner, suggesting the robustness of the phase transformation; this was in good agreement with the highly reversible electrochemical performance observed previously. The for-

mation of the overlithiated phase  $\text{Li}_{15+\theta}\text{Ge}_4$  and the amorphous phase  $\text{Li}_{3.5}\text{Ge}$  seemed to be a terminal process once the cell reached the end of the third discharge, as no significant change was observed in the spectra even when the cell potential was maintained at 0.005 V for 1 h (Figure 5ii). It is important to note that both phases vanished quickly once the electrical contact was removed (Figure 5iii–v), indicating that these two phases are electrically driven, metastable phases. The good reversibility in the charge/discharge cycles observed using  $^7\text{Li}$  NMR was consistent with the observed battery performance, and we can infer that the ability of the Ge@CNT composite to attain a high capacity may be associated with the presence of the overlithiated phase.

The electrically driven, reversible interconversion and coexistence of amorphous  $\text{Li}_{3.5}\text{Ge}$  and crystalline  $\text{Li}_{15}\text{Ge}_4$ /overlithiated  $\text{Li}_{15+\theta}\text{Ge}_4$  phase is a key electrochemical process underpinning the superior battery performance of Ge@CNT. The existence of the amorphous phase reduces the activation energy for lithium insertion and facilitates the recrystallization of  $\text{Li}_{15}\text{Ge}_4$  and extra insertion of  $\text{Li}^+$  to form overlithiated phase. The formation of the overlithiated phase allows the capacity of Ge@CNT to exceed the theoretical limitation of 1385 mAh g<sup>-1</sup>,<sup>42</sup> which is based on  $\text{Li}_{15}\text{Ge}_4$  as the terminal phase.  $\text{Li}_{15}\text{Ge}_4$  is an unusual electron-deficient phase which lacks one electron per formula unit ( $\text{Li}^{+15}\text{Ge}^{3.75-4}$ ),<sup>51</sup> thus it can accommodate extra charges. It has been reported that extra  $\text{Li}^+$  can be stored based on a “job sharing” mechanism in the crystalline defects or amorphous–crystalline interface.<sup>71</sup> Upon delithiation, there exists a kinetic barrier for the formation of a-Ge from crystalline  $\text{Li}_{15}\text{Ge}_4$ , since Ge–Ge bonds have been disrupted during the alloying. The existence of a- $\text{Li}_{3.5}\text{Ge}$  (with some residual Ge–Ge clusters) as well as sparsely distributed crystalline Ge nanodomains (observed in TEM) help to nucleate larger Ge domains and reduce the overpotential needed in the phase conversion.<sup>64</sup> Along with enhanced electrical conductivity provided by CNT, the improved ion-associated reaction kinetics facilitates reversibility of Ge@CNT especially under high current operation.

## CONCLUSIONS

In conclusion, we have synthesized Ge NRs encapsulated by bamboo-type multiwall CNTs. Ge@CNT delivers high capacity, superior rate capability (discharge in seconds), and good cycle stability. The unique structure of the CNT scaffold mechanically protects the Ge NRs from drastic volume swing during (de)lithiation processes and provides an effective model for multiprobe studies (TEM, XRD, and in situ NMR). Structural studies using TEM using coin-cell configuration, X-ray diffraction, and in situ  $^7\text{Li}$  NMR studies reveal that the reversibility of Li (de)lithiation in Ge@CNT during cycling is mediated by coexisting amorphous and crystalline phases. The high capacity observed may be related to electrically driven, metastable, overlithiated Li–Ge alloy, whose existence and reversibility depends on robust electrical interfaces afforded by the carbon walls encapsulating the Ge. The design and synthesis of such core–shell structure afford a generic strategy for protecting structurally unstable alloy phases in high energy and power density LIBs.

## EXPERIMENTAL SECTION

Details on the growth, electrochemical characterization, XRD, TEM, and in situ NMR studies are provided in the Supporting Information.

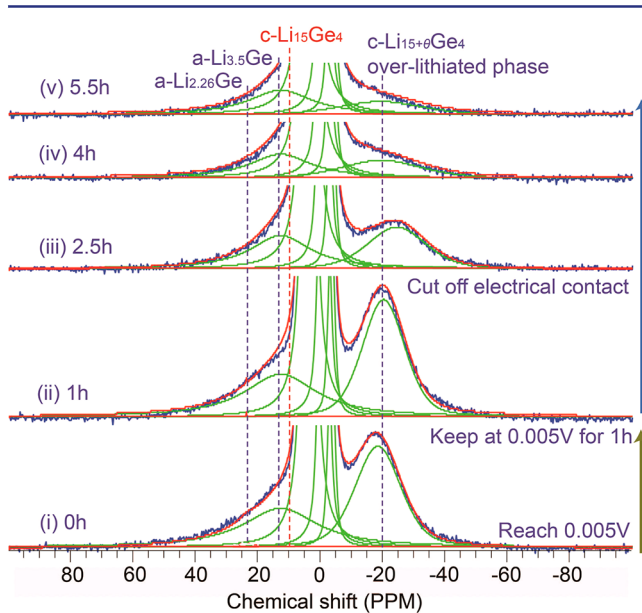


**Figure 5.** Stacked in situ  $^7\text{Li}$  NMR spectra of the Ge@CNT composite for the “electrical-off” experiment at the end of the third galvanostatic charge/discharge cycle. Once discharging had been completed at the end of the third cycle, the cell was maintained at 0.005 V for 1 h. After the external electrical contact was then removed, the overlithiated  $\text{Li}_{15+\theta}\text{Ge}_4$  phase vanished immediately. The broadening and positive shifting of the overlithiated phase peak may be attributed to the amorphization of Ge (see Figure 1g,h,i), which may speed the reaction kinetics of lithiation/delithiation.

**NMR Experiments.** The *in situ*  $^7\text{Li}$  NMR experiments were performed in a Varian-Agilent 300 MHz NMR spectrometer, corresponding to  $^7\text{Li}$  Larmor frequencies of 116.57 MHz. A homemade *in situ*  $^7\text{Li}$  NMR probe with a five-turn solenoid radiofrequency coil (internal diameter 12 mm), where the excitation magnetic field ( $B_1$ ) was perpendicular to the main magnetic field ( $B_0$ ), was used for the measurement. 1 M LiCl in distilled water was used as the reference (0 ppm). Each spectrum was acquired using a single pulse with a tip angle of  $45^\circ$  and pulse width of 4  $\mu\text{s}$ , an acquisition time of 30 ms, a recycle delay time of 1 s, and a total accumulation number of 256, corresponding to a total measurement time of about 4.4 min for each spectrum. For the specified charge–discharge current (0.18 mA) discussed above, a series of spectra were acquired consecutively.

The *in situ* NMR battery cell was a planar Li half-cell battery with the Ge@CNT composite as the working electrode and Li metal foil as the counter electrode. The composition and the preparation of the working electrode were exactly as described above. More details are provided in the Supporting Information.

## ■ ASSOCIATED CONTENT

### Supporting Information

Detailed synthetic process, electrochemical performance, and quantitative analysis of the phase compositions based on *in situ* NMR. This material is available free of charge via the Internet at <http://pubs.acs.org>.

## ■ AUTHOR INFORMATION

### Corresponding Authors

\*chmlohkp@nus.edu.sg

\*Jianzhi.Hu@pnnl.gov

\*m-lin@imre.a-star.edu.sg

### Notes

The authors declare no competing financial interest.

## ■ ACKNOWLEDGMENTS

MOE Tier II grant “Interface Engineering of Graphene Hybrids for Energy Conversion.” Grant no. R-143-000-488-112. *In-situ*  $^7\text{Li}$  NMR experiments were performed in the Environmental Molecular Sciences Laboratory, a national scientific user facility sponsored by the DOE’s Office of Biological and Environmental Research and located at Pacific Northwest National Laboratory (PNNL). PNNL is a multiprogram national laboratory operated for the DOE by Battelle Memorial Institute under contract DE-AC06-76RLO 1830. The authors receive assistance from Dr. Xilin Chen and Dr. Xiaolin Li in PNNL, Ms. Lili Liu, and Prof. Yuping Wu in Fudan University for conducting ball-milling and Dr. Tan Teck Leong in Institute of High Performance Computing (Singapore) for theoretical calculations.

## ■ REFERENCES

- (1) Wang, Y.; Lee, J. Y. *Angew. Chem., Int. Ed.* **2006**, *45*, 7039.
- (2) Zhang, W. M.; Hu, J. S.; Guo, Y.-G.; Zheng, S.-F.; Zhong, L.-S.; Song, W.-G.; Wan, L.-J. *Adv. Mater.* **2008**, *20*, 1160.
- (3) Xu, Y.; Liu, Q.; Zhu, Y.; Liu, Y.; Langrock, A.; Zachariah, M. R.; Wang, C. *Nano Lett.* **2013**, *13*, 470.
- (4) Seng, K. H.; Park, M.-H.; Guo, Z. P.; Liu, H. K.; Cho, J. *Angew. Chem., Int. Ed.* **2012**, *51*, 5.
- (5) Kim, H.; Son, Y.; Park, C.; Cho, J.; Choi, H. C. *Angew. Chem., Int. Ed.* **2013**, *52*, 5997.
- (6) Cui, G.; Gu, L.; Zhi, L.; Kaskhedikar, N.; van Aken, P. A.; Müllen, K.; Maier, J. *Adv. Mater.* **2008**, *20*, 3079.
- (7) Chan, C. K.; Zhang, X. F.; Cui, Y. *Nano Lett.* **2007**, *8*, 307.
- (8) Xue, D. J.; Xin, S.; Yan, Y.; Jiang, K.-C.; Yin, Y.-X.; Guo, Y.-G.; Wan, L.-J. *J. Am. Chem. Soc.* **2012**, *134*, 2512.
- (9) Kennedy, T.; Mullane, E.; Geaney, H.; Osiak, M.; O’Dwyer, C.; Ryan, K. M. *Nano Lett.* **2014**, *14*, 716.
- (10) Song, T.; Cheng, H.; Town, K.; Park, H.; Black, R. W.; Lee, S.; Park, W. I.; Huang, Y.; Rogers, J. A.; Nazar, L. F.; Paik, U. *Adv. Funct. Mater.* **2014**, *24*, 1458.
- (11) Magasinski, A.; Dixon, P.; Hertzberg, B.; Kvít, A.; Ayala, J.; Yushin, G. *Nat. Mater.* **2010**, *9*, 353.
- (12) Liu, N.; Lu, Z.; Zhao, J.; McDowell, M. T.; Lee, H.-W.; Zhao, W.; Cui, Y. *Nat. Nanotechnol.* **2014**, *9*, 187.
- (13) Guo, J.; Chen, X.; Wang, C. *J. Mater. Chem.* **2010**, *20*, 5035.
- (14) Luo, J.; Zhao, X.; Wu, J.; Jang, H. D.; Kung, H. H.; Huang, J. *J. Phys. Chem. Lett.* **2012**, *3*, 1824.
- (15) Chen, X.; Li, X.; Ding, F.; Xu, W.; Xiao, J.; Cao, Y.; Meduri, P.; Liu, J.; Graff, G. L.; Zhang, J.-G. *Nano Lett.* **2012**, *12*, 4124.
- (16) Yi, R.; Dai, F.; Gordin, M. L.; Sohn, H.; Wang, D. *Adv. Energy Mater.* **2013**, *3*, 1507.
- (17) Ge, M.; Lu, Y.; Ercius, P.; Rong, J.; Fang, X.; Mecklenburg, M.; Zhou, C. *Nano Lett.* **2013**, *14*, 261.
- (18) Park, C. M.; Kim, J. H.; Kim, H.; Sohn, H. *J. Chem. Soc. Rev.* **2010**, *39*, 3115.
- (19) Tarascon, J. M.; Armand, M. *Nature* **2001**, *414*, 359.
- (20) Goodenough, J. B. *Energy Environ. Sci.* **2014**, *7*, 14.
- (21) Yang, Z.; Zhang, J.; Kintner-Meyer, M. C. W.; Lu, X.; Choi, D.; Lemmon, J. P.; Liu, J. *Chem. Rev.* **2011**, *111*, 3577.
- (22) Yang, S.; Bachman, R. E.; Feng, X.; Müllen, K. *Acc. Chem. Res.* **2012**, *46*, 116.
- (23) Thackeray, M. M.; Wolverton, C.; Isaacs, E. D. *Energy Environ. Sci.* **2012**, *5*, 7854.
- (24) Wang, Y.; Wang, Y.; Hosono, E.; Wang, K.; Zhou, H. *Angew. Chem., Int. Ed.* **2008**, *47*, 7461.
- (25) Park, M.; Kim, K.; Kim, J.; Cho, J. *Adv. Mater.* **2010**, *22*, 415.
- (26) Seng, K. H.; Park, M.-h.; Guo, Z. P.; Liu, H. K.; Cho, J. *Nano Lett.* **2013**, *13*, 1230.
- (27) Sun, X.; Chen, T.; Yang, Z.; Peng, H. *Acc. Chem. Res.* **2012**, *46*, 539.
- (28) Lv, D.; Gordin, M. L.; Yi, R.; Xu, T.; Song, J.; Jiang, Y.; Choi, D.; Wang, D. *Adv. Funct. Mater.* **2014**, *24*, 1059.
- (29) Ren, J. G.; Wu, Q. H.; Tang, H.; Hong, G.; Zhang, W.; Lee, S. T. *J. Mater. Chem. A* **2013**, *1*, 1821.
- (30) Liu, J.; Song, K.; Zhu, C.; Chen, C.-C.; van Aken, P. A.; Maier, J.; Yu, Y. *ACS Nano* **2014**, *8*, 7051.
- (31) Cho, Y. J.; Im, H. S.; Kim, H. S.; Myung, Y.; Back, S. H.; Lim, Y. R.; Jung, C. S.; Jang, D. M.; Park, J.; Cha, E. H.; Cho, W. I.; Shojaei, F.; Kang, H. S. *ACS Nano* **2013**, *7*, 9075.
- (32) Cui, G.; Gu, L.; Kaskhedikar, N.; van Aken, P. A.; Maier, J. *Electrochim. Acta* **2010**, *55*, 985.
- (33) Li, W.; Yang, Z.; Cheng, J.; Zhong, X.; Gu, L.; Yu, Y. *Nanoscale* **2014**, *6*, 4532.
- (34) Yuan, F.-W.; Yang, H.-J.; Tuan, H.-Y. *ACS Nano* **2012**, *6*, 9932.
- (35) Seo, M. H.; Park, M.; Lee, K. T.; Kim, K.; Kim, J.; Cho, J. *Energy Environ. Sci.* **2011**, *4*, 425.
- (36) Yang, H.-J.; Tuan, H.-Y. *J. Mater. Chem.* **2012**, *22*, 2215.
- (37) Wang, D.; Chang, Y.-L.; Liu, Z.; Dai, H. *J. Am. Chem. Soc.* **2005**, *127*, 11871.
- (38) Tuan, H.-Y.; Lee, D. C.; Korgel, B. A. *Angew. Chem.* **2006**, *118*, 5308.
- (39) Yuan, F.-W.; Tuan, H.-Y. *Chem. Mater.* **2014**, *26*, 2172.
- (40) Pandurangan, A.; Morin, C.; Qian, D.; Andrews, R.; Crocker, M. *Carbon* **2009**, *47*, 1708.
- (41) Weker, J. N.; Liu, N.; Misra, S.; Andrews, J. C.; Cui, Y.; Toney, M. F. *Energy Environ. Sci.* **2014**, *7*, 2771.
- (42) Baggetto, L.; Notten, P. H. L. *J. Electrochem. Soc.* **2009**, *156*, A169.
- (43) Yoon, S.; Park, C.-M.; Sohn, H.-J. *Electrochem. Solid-State Lett.* **2008**, *11*, A42.
- (44) Lin, F.; Nordlund, D.; Weng, T.-C.; Zhu, Y.; Ban, C.; Richards, R. M.; L.Xin, H. *Nat. Commun.* **2014**, *5*, 3358.

- (45) Liu, X. H.; Huang, S.; Picraux, S. T.; Li, J.; Zhu, T.; Huang, J. Y. *Nano Lett.* **2011**, *11*, 3991.
- (46) Huang, J. Y.; Zhong, L.; Wang, C. M.; Sullivan, J. P.; Xu, W.; Zhang, L. Q.; Mao, S. X.; Hudak, N. S.; Liu, X. H.; Subramanian, A.; Fan, H.; Qi, L.; Kushima, A.; Li, J. *Science* **2010**, *330*, 1515.
- (47) Liu, X. H.; Wang, J. W.; Huang, S.; Fan, F.; Huang, X.; Liu, Y.; Krylyuk, S.; Yoo, J.; Dayeh, S. A.; Davydov, A. V.; Mao, S. X.; Picraux, S. T.; Zhang, S.; Li, J.; Zhu, T.; Huang, J. Y. *Nat. Nanotechnol.* **2012**, *7*, 749.
- (48) Gu, M.; Yang, H.; Perea, D. E.; Zhang, J.-G.; Zhang, S.; Wang, C. *Nano Lett.* **2014**, *14*, 4622.
- (49) Chevallier, F.; Letellier, M.; Morcrette, M.; Tarascon, J.-M.; Frackowiak, E.; Rouzaud, J.-N.; Béguin, F. *Electrochem. Solid-State Lett.* **2003**, *6*, A225.
- (50) Letellier, M.; Chevallier, F.; Béguin, F. *J. Phys. Chem. Solids* **2006**, *67*, 1228.
- (51) Key, B.; Bhattacharyya, R.; Morcrette, M.; Seznec, V.; Tarascon, J.-M.; Grey, C. P. *J. Am. Chem. Soc.* **2009**, *131*, 9239.
- (52) Ogata, K.; Salager, E.; Kerr, C. J.; Fraser, A. E.; Ducati, C.; Morris, A. J.; Hofmann, S.; Grey, C. P. *Nat. Commun.* **2014**, *5*, 3217.
- (53) Trill, J.-H.; Tao, C.; Winter, M.; Passerini, S.; Eckert, H. *J. Solid State Electrochem.* **2011**, *15*, 349.
- (54) Chen, H.; Hao, Q.; Zivkovic, O.; Hautier, G.; Du, L.-S.; Tang, Y.; Hu, Y.-Y.; Ma, X.; Grey, C. P.; Ceder, G. *Chem. Mater.* **2013**, *25*, 2777.
- (55) Wang, W. D.; Lucier, B. E. G.; Terskikh, V. V.; Wang, W.; Huang, Y. *J. Phys. Chem. Lett.* **2014**, *5*, 3360.
- (56) Feng, N.; Wang, Q.; Zheng, A.; Zhang, Z.; Fan, J.; Liu, S.-B.; Amoureaux, J.-P.; Deng, F. *J. Am. Chem. Soc.* **2013**, *135*, 1607.
- (57) Huo, H.; Chamas, M.; Lippens, P.-E.; Ménétrier, M. *J. Phys. Chem. C* **2012**, *116*, 2390.
- (58) Hata, K.; Futaba, D. N.; Mizuno, K.; Namai, T.; Yumura, M.; Iijima, S. *Science* **2004**, *306*, 1362.
- (59) Yan, C.; Xi, W.; Si, W.; Deng, J.; Schmidt, O. G. *Adv. Mater.* **2013**, *25*, 539.
- (60) Hwang, I. S.; Kim, J.-C.; Seo, S.-D.; Lee, S.; Lee, J.-H.; Kim, D.-W. *Chem. Commun.* **2012**, *48*, 7061.
- (61) Lee, H.; Kim, H.; Doo, S.-G.; Cho, J. *J. Electrochem. Soc.* **2007**, *154*, A343.
- (62) Lin, F.; Markus, I. M.; Nordlund, D.; Weng, T.-C.; Asta, M. D.; Xin, H. L.; Doeffer, M. M. *Nat. Commun.* **2014**, *5*, 3529.
- (63) Zhang, L. Q.; Liu, X. H.; Liu, Y.; Huang, S.; Zhu, T.; Gui, L.; Mao, S. X.; Ye, Z. Z.; Wang, C. M.; Sullivan, J. P.; Huang, J. Y. *ACS Nano* **2011**, *5*, 4800.
- (64) Key, B.; Morcrette, M.; Tarascon, J.-M.; Grey, C. P. *J. Am. Chem. Soc.* **2010**, *133*, 503.
- (65) Rangeet, B.; Baris, K.; Hailong, C.; Adam, S. B.; Anthony, F. H.; Clare, P. G. *Nat. Mater.* **2010**, *9*, 504.
- (66) Cattaneo, A. S.; Dupke, S.; Schmitz, A.; Badillo, J. P.; Winter, M.; Wiggers, H.; Eckert, H. *Solid State Ionics* **2013**, 249–250, 41.
- (67) Dinges, T.; Hoffmann, R.-D.; van Willen, L.; Henry, P.; Eckert, H.; Pöttgen, R. *J. Solid State Electrochem.* **2011**, *15*, 237.
- (68) Liu, X. H.; Zhang, L. Q.; Zhong, L.; Liu, Y.; Zheng, H.; Wang, J. W.; Cho, J.-H.; Dayeh, S. A.; Picraux, S. T.; Sullivan, J. P.; Mao, S. X.; Ye, Z. Z.; Huang, J. Y. *Nano Lett.* **2011**, *11*, 2251.
- (69) Liang, W.; Yang, H.; Fan, F.; Liu, Y.; Liu, X. H.; Huang, J. Y.; Zhu, T.; Zhang, S. *ACS Nano* **2013**, *7*, 3427.
- (70) McDowell, M. T.; Lee, S. W.; Nix, W. D.; Cui, Y. *Adv. Mater.* **2013**, *25*, 4966.
- (71) Maier, J. *Angew. Chem., Int. Ed.* **2013**, *52*, 4998.